How to Observe Coherent Electron Dynamics Directly

How to Observe Coherent Electron Dynamics Directly

Henri J. Suominen* and Adam Kirrander†
School of Chemistry, University of Edinburgh, West Mains Road, Edinburgh EH9 3JJ, United Kingdom
(Received 30 October 2013; published 30 January 2014)

Detection of electron motion by elastic scattering of short x-ray pulses from a coherent superposition of highly excited electronic states in rare gas atoms is investigated. The laser excitation of the electron wave packet introduces strong anisotropy which facilitates detection, and large differences in the radial distribution of the excited Rydberg and core electrons allow the dynamics to be detected using both soft and hard x rays.

DOI: 10.1103/PhysRevLett.112.043002 PACS numbers: 32.30.-r, 32.80.Ee, 34.80.Qb, 82.53.Hn

Imaging electron motion with spatial and temporal resolution could provide crucial understanding of many processes, such as photochemical reactions [1]. New x-ray free electron laser facilities, including LCLS [2], XFEL [3], SACLA [4], and FERMI [5], capable of short duration, tunable wave length x-ray pulses with high photon flux, will provide powerful tools for the imaging of matter, including ultrafast x-ray diffraction with spatial and temporal resolution [6,7]. Time-resolved x-ray diffraction capable of imaging atomic motion has already been demonstrated at third generation synchrotrons [8–10] for comparatively slow processes. Recently, diffraction from nanocrystals [11] and noncrystalline biological samples [12], as well as from isolated and strongly aligned gas phase molecules [13], has been observed using x-ray pulses at the LCLS. These advances set the stage for direct observation of electron motion.

One of the challenges to imaging electron motion is that the rapid dynamics of core and valence electrons, on the order of femtoseconds or less, may cause inelastic scattering to dominate the experimental signal [14,15]. However, Rydberg electron dynamics is slower and occurs on the order of picoseconds. Rydberg states play an important role in many gas phase chemical processes, and tunable Rydberg wave packets in atoms have been used widely to examine fundamental phenomena; examples include nondispersing Bohr wave packets [16], coherent control [17], and high harmonic generation [18]. In a prescient article, Wilson *et al.* [19] suggested that Rydberg wave packets in hydrogen atoms could be imaged using x-ray diffraction, with the electron wave packet forming a natural diffraction grid for the x-ray photon. Under very specific conditions, x-ray diffraction from extremely long-lived excited electronic states has already been demonstrated [20].

Rydberg electron wave packets in rare gas atoms exhibit complex dynamics, including the effects of electron correlation and quantum interferences, and have a number of important advantages that make them particularly suitable model systems for new diffraction experiments. It is straightforward to control the characteristic time scale of the dynamics by changing the excitation energy [21], and technologies exist to shape the wave packets [22,23]. The anisotropy induced by the optical excitation pulse increases the amount of information available. Most importantly, the dynamics can be recorded with both soft and hard x rays, measuring the complementary dynamics of the core-hole and Rydberg electrons. This makes it possible to use the entire range of x-ray energies available from new light sources, and effectively doubles the measurable signal.

We propose an experiment, shown schematically in Fig. 1, in which a pump laser excites a coherent wave packet in the atoms. The excited electrons are subsequently probed by an x-ray pulse with variable time delay between the pump and probe. For highly excited Rydberg states the dynamics is sufficiently slow that elastic kinematic scattering theory can be used to calculate the diffraction for x-ray energies away from atomic absorption edges [24,25],

$$\frac{d\sigma(\mathbf{s},t)}{d\Omega} = \frac{d\sigma_{\mathrm{Th}}}{d\Omega}\int \frac{I(t')}{\omega_{\mathbf{k}}}|f^0(\mathbf{s},t')|^2 dt', \tag{1}$$

where t is the pump-probe delay time, Ω the solid angle for scattering, $I(t')$ the x-ray pulse, $\omega_{\mathbf{k}}$ the energy of the incident x rays, and $d\sigma_{\mathrm{Th}}/d\Omega$ the Thomson scattering cross section for a free electron. Atomic units are used throughout. The momentum transfer vector, $\mathbf{s} = \mathbf{k}_0 - \mathbf{k}$, is defined as the difference between the incident and the scattered wave vectors, with $|\mathbf{k}| = |\mathbf{k}_0|$ for elastic scattering. The electron dynamics in the excited atoms enters Eq. (1) via the time-dependent scattering factor $f^0(\mathbf{s},t)$, which is calculated as

$$f^0(\mathbf{s},t) = \int \rho_{\mathrm{tot}}^{(N)}(\mathbf{r},t)e^{i\mathbf{s}\mathbf{r}}d\mathbf{r}. \tag{2}$$

The key quantity in Eq. (2) is the time-dependent N-electron density, $\rho_{\mathrm{tot}}^{(N)}(\mathbf{r},t)$, associated with the excited wave packet $|\Psi(\mathbf{r},t)\rangle$. The wave packet can be written as

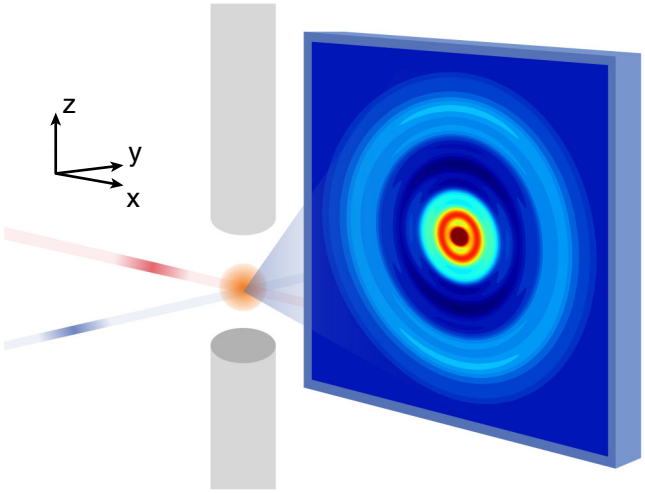

FIG. 1 (color online). Schematic of the experiment. The atoms are excited by a pump laser (red beam) and probed by an x-ray pulse (blue beam), with the diffracted x rays measured at a spatially resolved detector.

$$|\Psi(\mathbf{r},t)\rangle = \sum_i c_i e^{-\imath E_{is} t} |\Phi_i(\mathbf{r})\rangle, \tag{3}$$

where E_{is} is the energy relative the initial state s and $|\Phi_i(\mathbf{r})\rangle$ the stationary wave function. The expansion coefficients c_i are determined by the response of the atoms to the pump pulse. In the absence of multiphoton processes, these coefficients are given by first order perturbation theory, with $c_i = 2\pi\imath D_{is}\varepsilon(E_{is})$, where $\varepsilon(E)$ is the spectral profile of the pump pulse and D_{is} the state-specific dipole transition moment [21].

We now examine the structure of the wave packet in each atom in greater detail. The excited Rydberg states [26–28] consist of a positive ion core, essentially the $N-1$ electrons surrounding the nucleus, and a Rydberg electron that roams to large distances and repeatedly scatters from the positive ion core, exchanging energy and angular momentum with the core electrons in each collision. Conservation of energy and angular momentum leads to a set of channels, with each channel characterized by a combination of a core electronic state with a series of Rydberg electronic states that share the same angular momentum but have different principal quantum numbers.

The resulting time-dependent electron density $\rho^{(N)}_{\mathrm{tot}}(\mathbf{r},t)$ has three components, which correspond to the electron densities of the Rydberg electron, the $N-1$ electron ion core, and the N electron collision complex. These can be expanded as [29]

$$\rho^{(1)}_{r>r_c}(\mathbf{r},t) = \frac{1}{r^2}\sum_{j=1}^{N_c} |\mathbb{Y}_j(\vartheta,\phi)|^2 |\mathbb{R}_j(r,t)|^2, \tag{4a}$$

$$\rho^{(N-1)}_{r<r_c}(\mathbf{r},t) = \sum_{j=1}^{N_c} P_{j,r>r_c}(t)\rho^{(N-1)}_{j,r<r_c}(\mathbf{r}), \tag{4b}$$

$$\rho^{(N)}_{r<r_c}(\mathbf{r},t) = P_{r<r_c}(t)\rho^{(N)}_{r<r_c}(\mathbf{r}), \tag{4c}$$

where the sums run over the N_c dipole-allowed channels. The superscripts correspond to the number of electrons and the subscripts indicate the radial range, with r_c the radius of the electron-core collision complex. The Rydberg electron density, $\rho^{(1)}_{r>r_c}$ in Eq. (4a), is obtained from a time-dependent multichannel quantum defect theory calculation [21], with $\mathbb{Y}_j(\vartheta,\phi)$ the angular momentum function and $\mathbb{R}_j(r,t)$ the radial Rydberg electron wave packet. The core electron density, $\rho^{(N-1)}_{r<r_c}$ in Eq. (4b), consists of static core densities $\rho^{(N-1)}_{j,r<r_c}(\mathbf{r})$ from *ab initio* electronic structure calculations multiplied by the time-dependent probabilities $P_{j,r>r_c}(t)$, which correspond to the population in each channel defined by the probability of finding the Rydberg electron in a particular channel at a specific time $P_{j,r>r_c}(t) = \int_{r>r_c} |\mathbb{R}_j(r,t)|^2 dr$. The final component, the electron density of the collision complex in Eq. (4c), $\rho^{(N)}_{r<r_c}$, can be obtained from R-matrix calculations [27,28]. It is multiplied by the time-dependent probability that the Rydberg electron can be found inside the core $P_{r<r_c}(t)$, which is equivalent to the integrated probability flux of the Rydberg electron wave packet across the $r = r_c$ boundary surface [29]. It is worth noting that, apart from the factor $P_{r<r_c}(t)$, the $\rho^{(N)}_{r<r_c}$ density is *time independent*. This can be understood in terms of the weak energy dependence of the collision complex wave function, negligible over the bandwidth of the excitation pulse. For most Rydberg wave packets the collision complex makes a very small contribution to the x-ray diffraction pattern because $P_{r<r_c}(t) \ll 1$. From Eq. (4) and the associated discussion, we see that the recolliding Rydberg electron sets the relevant time scale and drives the dynamics of the highly excited atom.

For the Rydberg electron, the jj-coupled angular momentum function $\mathbb{Y}_j(\vartheta,\varphi)$ in Eq. (4a) is a sum of spherical harmonics $Y_{l_j m_l}$ with different m_l, such that

$$|\mathbb{Y}_j(\vartheta,\phi)|^2 = \sum_{m_l,m_s} \langle J_c j_e M_c m_e | JM\rangle^2 \langle l_j s m_l m_s | j_e m_e\rangle^2 \times |Y_{l_j m_l}(\vartheta,\varphi)|^2, \tag{5}$$

with $|m_l| \le l_j$ and $m_s = \pm\frac{1}{2}$, where J is the total angular momentum and where J_c and j_e are the total angular momenta of the core and the Rydberg electron, respectively. The important point is that the angular momentum coupling matches the spatial structure of the core electron-hole configuration with that of the Rydberg electron. The angular wave function of the core and the Rydberg electron are thus intrinsically linked, and time-dependent diffraction from the core and the Rydberg electron provide complementary information about the *same* dynamic process, albeit at very different length scales.

In rare gas atoms, the positive ion core has an open shell structure that supports a large number of channels with

complicated angular momentum coupling. This leads to complex multichannel Rydberg dynamics with an anisotropic diffraction signal, which is easier to detect against the isotropic background diffraction from ground state $^1S_0$ rare gas atoms and spherically symmetric inner shell core electrons. Helium and neon have the smallest number of active channels, and very high ionization energies that make excitation of Rydberg states difficult [30]. The heavier rare gas elements, including argon, krypton, and xenon, all have five channels that are allowed by dipole selection rules. Among these, argon has the smallest number of closed-shell electrons and, thus, the least isotropic background diffraction.

Excitation by a linearly polarized photon from the closed-shell $^1S_0$ ground state of argon results in excited states with total angular momentum $J = 1$ and projection $M = 0$. The jj-coupled channels are identified by the state of the positive ion core and corresponding state of the Rydberg electron, $^2P^\circ_{3/2}$ $(s_{1/2}, d_{3/2}, d_{5/2})$, referred to as channels 1–3, and $^2P^\circ_{1/2}$ $(s_{1/2}, d_{3/2})$, referred to as channels 4 and 5. The three first series converge on the $^2P^\circ_{3/2}$ ground state of the ion at energy 15.760 eV, and two final series on the first excited $^2P^\circ_{1/2}$ state of the ion at energy 15.937 eV. We use the **K** matrix and dipole transition moments from the relativistic spin-orbit coupled *ab initio* calculations by Johnson *et al.* [31], which account for correlation within and between $3s$ and $3p$ shells while the inner shells are treated in a frozen core approximation. The calculated energy levels match spectroscopic measurements [32] closely across a wide range of energies. The electronic structure of the Ar^+ core states is calculated using the *ab initio* package MOLPRO [33]. The weak hyperfine coupling is not included since the most abundant isotopes of Ar have zero nuclear spin.

A pump pulse with 1.5 ps duration (10 cm^{-1} FWHM bandwidth) excites a wave packet centered at energy 15.717 eV, below the lowest ionization potential. Excitation to the $J = 1$ Rydberg states can be achieved via single-photon excitation or via a resonant multiphoton process with a $J = 0$ intermediate state [17,34]. Figure 2 shows the proportional contribution of each of the five channels to the total wave packet as a function of time, via the probability $P_{j,r>r_c}(t)$ in Eq. (4b). Figure 2 does not include the population of the collision complex, corresponding to term $P_{r<r_c}(t)$ in Eq. (4c), which remains $< 0.5\%$ of the total population throughout. The slowest beat in the system is the flow of probability between channels 3 and 4, changing the electronic state of the core and the orbital angular momentum of the Rydberg electron over a time period of approximately 35 ps. There are two faster transitions that change the electronic state of the core, but not the orbital angular momentum of the Rydberg electron. First, population flows between channels 1 and 4 over a period of 4.3 ps, and second, between channels 2 and 5 with a period of 2.2 ps. In terms of the electronic state of the core,

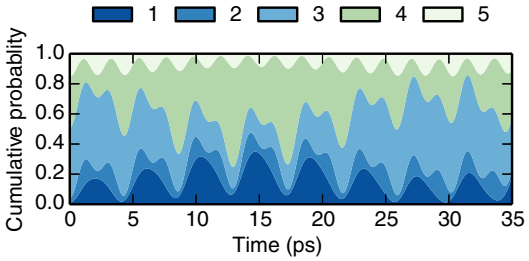

FIG. 2 (color online). Composition of the wave packet across channels 1–5 as a function of time (see text for details).

at 13 ps the population of the $^2P^\circ_{1/2}$ core (channels 4–5) reaches a maximum of 75%, while the $^2P^\circ_{3/2}$ core (channels 1–3) has a maximum population of 85% after 28 ps.

Figure 3 shows the radial probability density as a function of time in a multichannel version of a quantum carpet [35]. The radial density has a distinct nodal structure, with the inner nodes in the $^2P^\circ_{3/2}$ channels spaced by 15 au and the outer nodes spaced by 85 au. For the $^2P^\circ_{1/2}$ channels the corresponding distances are 10 to 30 au. It is worth noting that the positions of the nodes do not change throughout the dynamics, which is a consequence of the comparatively narrow-band excitation pulse. Since the core is in a higher-energy electronic state for the $^2P^\circ_{1/2}$ channels, in these channels the more tightly bound Rydberg electron has a small classical radius 124 au, significantly less than the radius 638 au in the $^2P^\circ_{3/2}$ channels. The difference in outer radius can be seen clearly in Fig. 3. As a consequence, the atom undergoes dramatic changes in overall size as population flows between the $^2P^\circ_{3/2}$ and the $^2P^\circ_{1/2}$ channels. This is apparent when comparing the Rydberg electron density in Fig. 4(e) with Figs. 4(d) and 4(f).

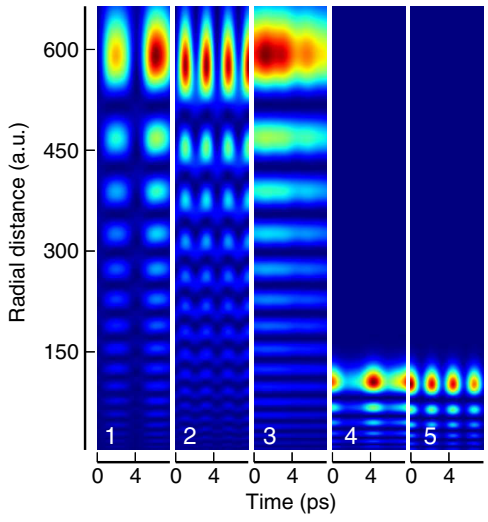

FIG. 3 (color online). Radial density, $|\mathbb{R}_j(r,t)|^2$ in Eq. (4a), for the wave packet plotted as a function of time (0–8 ps) and radial distance in each channel 1–5.

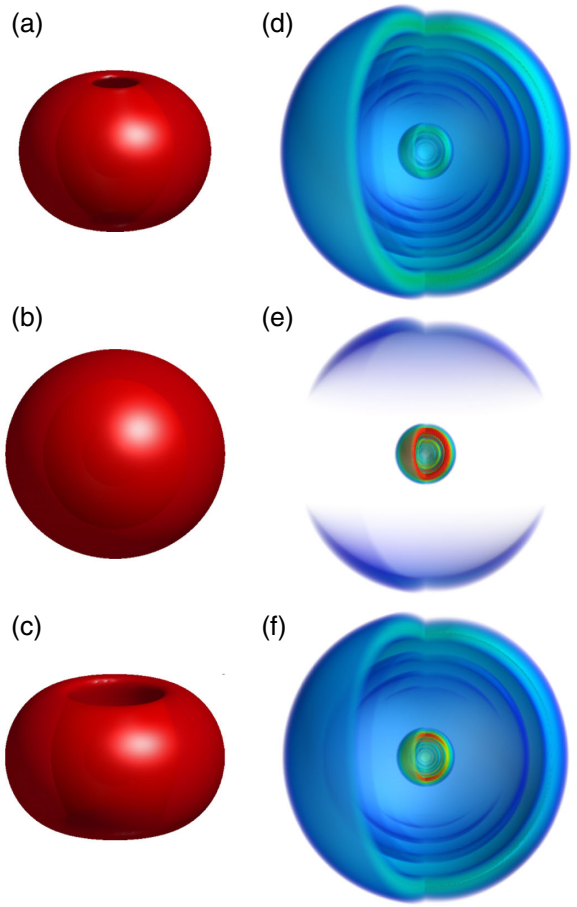

FIG. 4 (color online). Electron density isosurfaces at times 5.6 ps (a),(d), 12.7 ps (b),(e), and 19.3 ps (c),(f). (a)–(c) Core-hole density. (d)–(f) Rydberg electron density. The Rydberg radius is 2 orders of magnitude larger than the core (images not to scale).

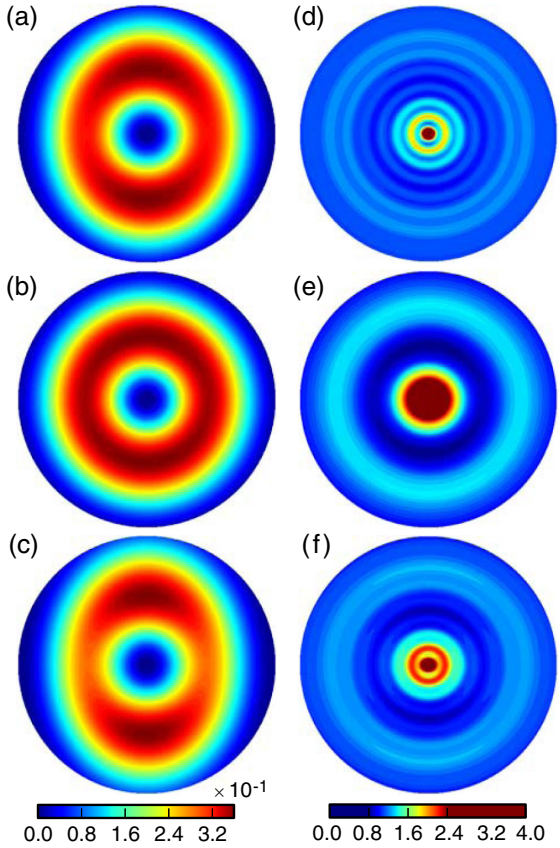

FIG. 5 (color online). Diffraction patterns at 5.6 ps (a),(d), 12.7 ps (b),(e), and 19.3 ps (c),(f). (a)–(c) 9.5 keV photons, showing $|sf^0(\mathbf{s},t)|^2$ for radial scattering angle $\theta \leq 36^\circ$. (d)–(f) 280 eV photons, showing $|f^0(\mathbf{s},t)|^2$ for $\theta \leq 72^\circ$. See also the Supplemental Material [36].

Figure 4 shows the time-dependent electron density at three times (5.6, 12.7, and 19.3 ps). Figures 4(a)–4(c) show the single-electron-equivalent core hole, essentially $\rho^{(N-1)}_{r<r_c}(\mathbf{r},t)$ in Eq. (4b) with the $N-2$ inert electrons subtracted, and Figs. 4(d)–4(f) the scaled Rydberg electron density, $r^2\rho^{(1)}_{r>r_c}(\mathbf{r},t)$ from Eq. (4a). As the channel populations change with time, so does the shape, size, and angular distribution of the electron density. At 5.6 ps, the core density is asymmetric [Fig. 4(a)], while the Rydberg electron density is evenly distributed in symmetric shells [Fig. 4(d)]. Then at 12.7 ps, the *core* is symmetric [Fig. 4(b)], while the Rydberg density is concentrated in the compact $^2P^\circ_{1/2}$ channels [Fig. 4(e)]. Finally, at 19.3 ps, both the core [Fig. 4(c)] and the Rydberg electron [Fig. 4(f)] densities are asymmetric.

We calculate the diffraction via the differential cross section in Eq. (1). In Fig. 5 the total diffraction is shown at three pump-probe delay times, 5.6, 12.7, and 19.3 ps, corresponding to the three times included in Fig. 4. At each time, the diffraction is calculated for two x-ray probe wavelengths, 9.5 keV (1.3 Å) and 280 eV (44.3 Å), corresponding to the upper and lower end of the fundamental at LCLS [2]. The pulse duration is 100 fs, giving an essentially instantaneous diffraction pattern (see the Supplemental Material [36]). For the 9.5 keV x rays, the pattern is dominated by diffraction from the core and, because the diffraction falls off rapidly with radial scattering angle θ, is presented as $|sf^0(\mathbf{s},t)|^2$. The diffraction reflects the shape of the core, with an asymmetric pattern at 5.6 ps, symmetric at 12.7 ps, and finally asymmetric again at 19.3 ps. For the 280 eV x-ray probe, the diffraction pattern, shown as $|f^0(\mathbf{s},t)|^2$, is dominated by the Rydberg electron. A distinct ring structure is present in the diffraction pattern due to the nodes in the Rydberg electron density (see Fig. 4). The diffraction pattern consists of many symmetric rings at 5.6 ps [Fig. 5(d)], a small number of broad rings at 12.7 ps [Fig. 5(e)], and finally a somewhat asymmetric pattern at 19.3 ps [Fig. 5(f)]. The static and spherically symmetric background diffraction due to the inert $N-2$ core electrons is shown in the Supplemental Material [36].

The main experimental parameters are the number of incident x-ray photons N_λ and the number of atoms in the

sample N_{at}. The number of diffracted photons is proportional to $N_\lambda N_{at}\sigma_T|f^0(\mathbf{s},t)|^2$, where σ_{Th} is the total Thomson cross section and $|f^0(\mathbf{s},t)|^2$ the diffraction amplitude. For a sample of 10^{15} atoms and an x-ray pulse with intensity 10^{16} W/cm^2 and duration 100 fs, the number of usefully diffracted photons per pulse is on the order of 10^2. Since the photoelectric cross sections are greater at low energies, this may favor diffraction with higher energy x-ray photons. The experiments are sensitive to fluctuations in the x-ray pulses or jitter in the timing of the optical pump and the x-ray probe, but effective diagnostics have been developed to overcome these difficulties [2,6,36].

In conclusion, the proposed experiments would allow direct visualization of electron correlation effects and wave packet dynamics. An alternative approach based on nonlinear optical processes has shown promise in recent years [37–40], but the intense infrared fields used strongly perturb the dynamics [41], and ultrafast diffraction has the potential to be a less invasive technique. Ultrafast diffraction capable of resolving electronic changes during chemical reactions presents enormous potential to advance our understanding of photochemistry. The development of such experiments is challenging, but Rydberg wave packets in rare gas atoms should serve as ideal model systems for this endeavor.

Funding from the European Community (FP7-PEOPLE-2013-CIG-NEWLIGHT) and helpful discussions with Dr. G. Dixit (Max Born Institute) are gratefully acknowledged.

*Present address: Center for Quantum Devices, Niels Bohr Institute, University of Copenhagen, Universitetsparken 5, 2100 Copenhagen, Denmark.
†Adam.Kirrander@ed.ac.uk

[1] A. Stolow, Discuss. Faraday Soc. **163**, 9 (2013).
[2] C. Bostedt *et al.*, J. Phys. B **46**, 164003 (2013).
[3] J. Feldhaus, M. Krikunova, M. Meyer, Th. Möller, R. Moshammer, A. Rudenko, Th. Tschentscher, and J. Ullrich, J. Phys. B **46**, 164002 (2013).
[4] M. Yabashi *et al.*, J. Phys. B **46**, 164001 (2013).
[5] V. Lyamayev *et al.*, J. Phys. B **46**, 164007 (2013).
[6] J. Ullrich, A. Rudenko, and R. Moshammer, Annu. Rev. Phys. Chem. **63**, 635 (2012).
[7] J. Kim, K. H. Kim, J. H. Lee, and H. Ihee, Acta Crystallogr. Sect. A **66**, 270 (2010).
[8] R. Neutze *et al.*, Phys. Rev. Lett. **87**, 195508 (2001).
[9] J. Davidsson *et al.*, Phys. Rev. Lett. **94**, 245503 (2005).
[10] Q. Kong *et al.*, Acta Crystallogr. Sect. A **66**, 252 (2010).
[11] H. N. Chapman *et al.*, Nature (London) **470**, 73 (2011).
[12] M. M. Seibert *et al.*, Nature (London) **470**, 78 (2011).
[13] J. Küpper *et al.*, arXiv:1307.4577.
[14] G. Dixit, O. Vendrell, and R. Santra, Proc. Natl. Acad. Sci. U.S.A. **109**, 11636 (2012).
[15] G. Dixit and R. Santra, J. Chem. Phys. **138**, 134311 (2013).
[16] H. Maeda, J. H. Gurian, and T. F. Gallagher, Phys. Rev. Lett. **102**, 103001 (2009).
[17] J. R. R. Verlet, V. G. Stavros, R. S. Minns, and H. H. Fielding, Phys. Rev. Lett. **89**, 263004 (2002).
[18] A. Gürtler, F. Robicheaux, M. J. J. Vrakking, W. J. van der Zande, and L. D. Noordam, Phys. Rev. Lett. **92**, 063901 (2004).
[19] J. L. Krause, K. J. Schafer, M. Ben-Nun, and K. R. Wilson, Phys. Rev. Lett. **79**, 4978 (1997).
[20] M. R. Pressprich, M. A. White, Y. Vekhter, and P. Coppens, J. Am. Chem. Soc. **116**, 5233 (1994).
[21] A. Kirrander, H. H. Fielding, and Ch. Jungen, J. Chem. Phys. **127**, 164301 (2007).
[22] T. C. Weinacht, J. Ahn, and P. H. Bucksbaum, Phys. Rev. Lett. **80**, 5508 (1998).
[23] T. C. Weinacht, J. Ahn, and P. H. Bucksbaum, Nature (London) **397**, 233 (1999).
[24] K. B. Møller and N. E. Henriksen, Struct. Bond. **142**, 185 (2012).
[25] N. E. Henriksen and K. B. Møller, J. Phys. Chem. B **112**, 558 (2008).
[26] T. F. Gallagher, *Rydberg Atoms* (Cambridge University Press, Cambridge, England, 1994), 1st ed.
[27] M. Aymar, C. H. Greene, and E. Luc-Koenig, Rev. Mod. Phys. **68**, 1015 (1996).
[28] P. G. Burke and K. A. Berrington, *Atomic and Molecular Processes: An R-Matrix Approach* (IOP Publishing, Bristol, England, 1993).
[29] A. Kirrander, J. Chem. Phys. **137**, 154310 (2012).
[30] M. Grütter, O. Zehnder, T. P. Softley, and F. Merkt, J. Phys. B **41**, 115001 (2008).
[31] W. R. Johnson, K. T. Cheng, K.-N. Huang, and M. Le Dourneuf, Phys. Rev. A **22**, 989 (1980).
[32] A. Kramida, A. Yu. Ralchenko, and J. Reader (NIST ASD Team), *NIST Atomic Spectra Database* (National Institute of Standards and Technology, Gaithersburg, MD, 2012), http://www.nist.gov/pml/data/atomspec.cfm.
[33] H.-J. Werner, P. J. Knowles, G. Knizia, F. R. Manby, M. Schütz, *et al.*, MOLPRO v.2012.1, a package of *ab initio* programs.
[34] V. L. Sukhorukov, I. D. Petrov, M. Schäfer, F. Merkt, M.-W. Ruf, and H. Hotop, J. Phys. B **45**, 092001 (2012).
[35] P. Kazemi, S. Chaturvedi, I. Marzoli, R. F. O'Connell, and W. P. Schleich, New J. Phys. **15**, 013052 (2013).
[36] See Supplemental Material at http://link.aps.org/supplemental/10.1103/PhysRevLett.112.043002 for details on the dynamics, the x-ray scattering, and selected experimental considerations.
[37] E. Goulielmakis *et al.*, Nature (London) **466**, 739 (2010).
[38] S. Haessler *et al.*, Nat. Phys. **6**, 200 (2010).
[39] P. Hockett, C. Z. Bisgaard, O. J. Clarkin, and A. Stolow, Nat. Phys. **7**, 612 (2011).
[40] P. Tzallas, E. Skantzakis, L. A. A. Nikolopoulos, G. D. Tsakiris, and D. Charalambidis, Nat. Phys. **7**, 781 (2011).
[41] B. J. Sussman, D. Townsend, M. Y. Ivanov, and A. Stolow, Science **314**, 278 (2006).